

Message-Passing Neural Quantum States for the Homogeneous Electron Gas

Gabriel Pescia,^{1,2} Jannes Nys,^{1,2} Jane Kim,³ Alessandro Lovato,^{4,5,6} and Giuseppe Carleo^{1,2}

¹*Institute of Physics, École Polytechnique Fédérale de Lausanne (EPFL), CH-1015 Lausanne, Switzerland*

²*Center for Quantum Science and Engineering, École Polytechnique Fédérale de Lausanne (EPFL), CH-1015 Lausanne, Switzerland*

³*Department of Physics and Astronomy and Facility for Rare Isotope Beams, Michigan State University, East Lansing, Michigan 48824, USA*

⁴*Physics Division, Argonne National Laboratory, Argonne, Illinois 60439*

⁵*Computational Science Division, Argonne National Laboratory, Argonne, Illinois 60439*

⁶*INFN-TIFPA Trento Institute for Fundamental Physics and Applications, 38123 Trento, Italy*

(Dated: May 15, 2023)

We introduce a neural-network-based wave function Ansatz to accurately simulate extended, strongly interacting fermions in continuous space. The variational state is parameterized via permutation-equivariant message-passing neural networks to transform single-particle coordinates into highly correlated quasi-particle coordinates. We show the versatility and accuracy of this Ansatz by simulating the ground state of the homogeneous electron gas in three spatial dimensions at different densities and system sizes. Our model respects the fundamental symmetries of the Hamiltonian, such as continuous translation symmetries. We show better or comparable ground-state energies on small benchmark systems, compared to current state-of-the-art neural-network wave functions, using orders of magnitudes less variational parameters and optimization steps. These savings allow us to scale up to system sizes of $N = 128$ electrons, previously inaccessible to neural-network wave functions in continuous space, opening the door for future work on finite-size extrapolations to the thermodynamic limit. We investigate the Ansatz's capability of identifying and representing different phases of matter without imposing any structural bias toward a given phase.

I. INTRODUCTION

Predicting emergent physical phenomena and system properties from the ab initio description of the system's constituents is a notoriously difficult task [1, 2]. Fermionic systems, in particular, can exhibit strong correlations among the particles, leading to surprising collective phenomena in the form of exotic phases of matter, e.g. superconductivity and superfluidity [3, 4].

In recent years, progress in numerical simulations of strongly correlated systems has been triggered by the development of increasingly precise approximation techniques from machine learning. Most notably, artificial neural network (NN) architectures, in combination with Variational Monte Carlo (VMC), have shown great promise to represent ground states of quantum spin systems, especially in more than one spatial dimension [5–12]. The universal approximation property of NNs guarantees that neural-network quantum states (NQS) can, in theory, accurately represent any quantum many-body state [13, 14]. These techniques have been extended to fermionic degrees of freedom in a discrete basis [15–17], by incorporating the indistinguishability of quantum particles. More recently, the scope of NQS methods has also been broadened to the realm of ground and excited state searches for fermionic and bosonic continuous degrees of freedom with open [18–20] and periodic boundary conditions (PBCs) [21–23].

The great flexibility of NQS, compared to more traditional models, allows representing multiple phases of matter, system sizes, and even different physical systems. To exemplify this point, we refer to NQS studies on the

ground-state of molecular systems [18, 19], solutions to effective field theory Hamiltonians describing atomic nuclei [24–26], studies of the bulk of fermionic and bosonic extended systems [21, 23, 27, 28], as well as the NQS simulation of low-density neutron matter found in neutron stars [29]. The downside of these favorable properties of current architectures in continuous space is that they typically need a significant amount of variational parameters to reach a given accuracy. This makes the optimization procedure challenging and costly, preventing the usage of refined optimization schemes, e.g. second order optimization procedures [30, 31]. As a result, the system sizes that can be studied nowadays are limited to a few tens of particles. However, accessing larger system sizes is of utmost importance to estimate physical properties in the thermodynamic limit [32–35]. To remedy the situation, novel NQS architectures must be developed that significantly reduce the parameter complexity while retaining high accuracy.

This work introduces a continuous-space NQS suitable for simulating strongly interacting fermionic quantum systems with a favorable scaling of the number of variational parameters. The Ansatz uses a permutation-equivariant message-passing architecture on a graph that inherently implements the indistinguishability of same-species quantum particles [36], thus we refer to it as Message-Passing Neural Quantum State (MP-NQS). Additionally, we show that we can impose spatial and spin symmetries of the system into our model. Our architecture allows us to reduce the number of variational parameters by *one to two orders of magnitude* compared to other well-known NQS for continuous space. This,

in turn, opens up the possibility to use the Stochastic Reconfiguration (SR) optimization technique [31], which lowers the number of optimization steps needed to reach convergence by about *two orders of magnitude*, while reaching similar or better accuracy.

II. METHODS

A. Exact Wave Functions and Mean-Value Point

Finding the ground state wave function of a strongly interacting Hamiltonian is generally a complex task that only admits analytical solutions in special cases. However, we argue in the following that the exact ground-state wave function obeys a general functional structure. We consider an arbitrary non-relativistic Hamiltonian of identical particles of mass m in d spatial dimensions:

$$H = -\frac{\hbar^2}{2m} \sum_i^N \nabla_{\mathbf{r}_i}^2 + V(\mathbf{X}), \quad (1)$$

where the potential and interaction energy V is assumed to be diagonal in position representation, defined by the particle coordinates $\mathbf{X} = (\mathbf{r}_1, \dots, \mathbf{r}_N)$ (with $\mathbf{r}_i \in \mathbb{R}^d$). We also introduce a suitable reference state $|\Phi_0\rangle$, taken as an initial condition for the imaginary-time (τ) evolution induced by the Hamiltonian:

$$\Phi_\tau(\mathbf{X}) = \langle \mathbf{X} | e^{-\tau H} | \Phi_0 \rangle \quad (2)$$

It is well known that the exact ground-state wave function is obtained in the limit of large imaginary times: $\lim_{\tau \rightarrow \infty} \Phi_\tau(\mathbf{X}) \propto \Psi_0(\mathbf{X})$, provided that the initial state $|\Phi_0\rangle$ is non-orthogonal to the exact ground state, $|\langle \Psi_0 | \Phi_0 \rangle| > 0$. The non-orthogonality condition, in the fermionic case, also implies that the wave function must be antisymmetric $\Phi_0(\mathcal{P}_{ij}(\mathbf{X})) = -\Phi_0(\mathbf{X})$ under the exchange of any two particles $i \leftrightarrow j$, as performed by the operator \mathcal{P}_{ij} . To make progress on the explicit functional form of Eq. (2), we write

$$\Phi_\tau(\mathbf{X}) = \int_{\Omega} d\mathbf{X}' G_\tau(\mathbf{X}, \mathbf{X}') \Phi_0(\mathbf{X}') \quad (3)$$

$$= \text{Vol}(\Omega) \times G_\tau(\mathbf{X}, \mathbf{Y}(\mathbf{X})) \Phi_0(\mathbf{Y}(\mathbf{X})), \quad (4)$$

where Ω is a suitable integration domain for the positional degrees of freedom, and $G_\tau(\mathbf{X}, \mathbf{X}') = \langle \mathbf{X} | e^{-\tau H} | \mathbf{X}' \rangle$ is the matrix element of the imaginary-time propagator. In the second line above, we have used the mean-value theorem for integrals, which states that under relatively mild smoothness conditions, the value of the integral is proportional to the value of the integrand computed at a point belonging to the integration domain. We call this special point $\mathbf{Y}(\mathbf{X}) = (\mathbf{y}_1(\mathbf{X}), \dots, \mathbf{y}_N(\mathbf{X}))$, since the value

of the integral depends parametrically on the coordinates \mathbf{X} .

In the general case of a non-relativistic Hamiltonian, Eq. (1), it can be shown that $G_\tau(\mathbf{X}, \mathbf{X}') \geq 0$ for all values of \mathbf{X}, \mathbf{X}' . Moreover, the propagator is invariant under the exchange of particle coordinates: $G_\tau(\mathcal{P}_{ij}(\mathbf{X}), \mathcal{P}_{ij}(\mathbf{X}')) = G_\tau(\mathbf{X}, \mathbf{X}')$. For fermionic wave functions, this invariance implies that $\mathbf{Y}(\mathbf{X})$ must be equivariant under particle exchange, $\mathbf{Y}(\mathcal{P}_{ij}(\mathbf{X})) = \mathcal{P}_{ij}(\mathbf{Y}(\mathbf{X}))$, such that the resulting total wave function remains antisymmetric. The functional form found is then the product of a permutationally symmetric and positive semi-definite function $J(\mathbf{X}) = G_\tau(\mathbf{X}, \mathbf{Y}(\mathbf{X})) \times \text{Vol}(\Omega)$ and the reference state computed at modified coordinates $\mathbf{Y}(\mathbf{X})$:

$$\Phi_\tau(\mathbf{X}) = J(\mathbf{X}) \times \Phi_0(\mathbf{Y}(\mathbf{X})). \quad (5)$$

The many-body coordinate transformation entering the amplitudes of the initial state coincides with the mean-value point of the integrand in our derivation and is an alternative justification for the backflow transformation [37] of single-particle coordinates.

In the simple case in which the initial state is a Slater determinant of given spin orbitals $\phi_\mu(\mathbf{r}_i)$, one has that $\Phi_0(\mathbf{X}) = \det\{\phi_\mu(\mathbf{r}_i)\} / \sqrt{N!}$. The functional form, resulting from Eq. (5), is then structurally related to the heuristic Jastrow-Backflow variational form [38, 39]. We can also remark that the permutation-invariant contribution can be absorbed inside the determinant such that

$$\Phi_\tau(\mathbf{X}) = \mathcal{K} \times \det\{\varphi_\mu(\mathbf{y}_i(\mathbf{X}))\}, \quad (6)$$

with $\varphi_\mu(\mathbf{y}_i(\mathbf{X})) = \phi_\mu(\mathbf{y}_i(\mathbf{X})) \times \sqrt[3]{J(\mathbf{X})}$, and \mathcal{K} a normalization constant. In principle, the functional form above is exact, provided that the symmetric factor $J(\mathbf{X})$ and the mean-value coordinates $\mathbf{Y}(\mathbf{X})$ are chosen to satisfy Eq. (4), and the reference state is not orthogonal to the true ground state. An approximate but explicit form for the coordinate transformation $\mathbf{Y}(\mathbf{X})$ can be obtained by repeatedly applying the imaginary-time propagator to the reference state in the limit of small τ . This process gives rise to the concept of an iterative backflow transformation, as introduced in Ref. [40].

B. Message-Passing Neural Quantum State

Motivated by the functional form of Eq. (6), we construct our variational Ansatz by combining simple single-particle orbitals, $\{\phi_\mu\}_{\mu=1}^N$, with highly correlated many-body backflow coordinates, $\mathbf{Y}(\mathbf{X})$. The backflow transformation is parameterized using highly flexible, permutation-equivariant message-passing neural networks (MPNN) [36] (see Fig. 1) that can be structurally related to the iterative backflow approach [40, 41].

At each iteration t of the network, we build a graph consisting of vectors that encode effective particle positions (nodes) $\mathbf{x}_i^{(t)} \in \mathbb{R}^{D_1}$ and their interactions (edges)

$\mathbf{x}_{ij}^{(t)} \in \mathbb{R}^{D_2}$, with suitably chosen *feature* dimensions D_1 and D_2 . Starting from a given graph, we then construct messages from its edges $\mathbf{x}_{ij}^{(t)}$:

$$\mathbf{m}_{ij}^{(t+1)} = \omega_{ij}^{(t)}(\mathbf{x}_{ij}^{(t)}) \odot \phi(\mathbf{x}_{ij}^{(t)}) \quad (7)$$

where \odot represents element-wise multiplication over the dimension D_2 and weight vectors $\omega_{ij}^{(t)} \in \mathbb{R}^{D_2}$ are introduced. These weights are computed using a variant of the attention mechanism introduced in [42]. First we transform the *edge-features* $\mathbf{x}_{ij}^{(t)}$ to query/key matrices $\mathbf{Q}_{ij}^{(t)} = W_Q^{(t)} \cdot \mathbf{x}_{ij}^{(t)}$ and $\mathbf{K}_{ij}^{(t)} = W_K^{(t)} \cdot \mathbf{x}_{ij}^{(t)}$, respectively, using weight matrices $W_Q^{(t)}, W_K^{(t)} \in \mathbb{R}^{D_2 \times D_2}$. We proceed to compute the overlap between these queries and keys *along the particle dimension* (as opposed to the feature dimension [42, 43]) and apply an element-wise GELU non-linearity [44]. As a result, we obtain the permutation-equivariant weights

$$\omega_{ij}^{(t)} = \text{GELU} \left(\sum_l \mathbf{Q}_{il}^{(t)} \mathbf{K}_{lj}^{(t)} \right). \quad (8)$$

The above attention mechanism compares the environments of particle i and j , and effectively increases the order of correlations that can be embedded in the messages within one iteration of the network. The higher-order correlations induced by the attention mechanism are crucial to reducing network iterations and capturing many-body effects.

In addition to nodes $\mathbf{x}_i^{(t)}$ and edges $\mathbf{x}_{ij}^{(t)}$, the MPNN also carries along and updates auxiliary variables known as hidden states, both on nodes ($\mathbf{h}_i^{(t)} \in \mathbb{R}^{D_1^h}$) and on edges ($\mathbf{h}_{ij}^{(t)} \in \mathbb{R}^{D_2^h}$). The messages, as constructed above, are used to update the hidden states of the feature vectors:

$$\mathbf{h}_i^{(t+1)} = \mathbf{f} \left(\mathbf{x}_i^{(t)}, \sum_{j \neq i} \mathbf{m}_{ij}^{(t+1)} \right) \quad (9)$$

$$\mathbf{h}_{ij}^{(t+1)} = \mathbf{g} \left(\mathbf{x}_{ij}^{(t)}, \mathbf{m}_{ij}^{(t+1)} \right) \quad (10)$$

The functions ϕ , \mathbf{f} , and \mathbf{g} introduced above are parameterized by Multilayer Perceptrons (MLPs). We build a new graph with the same structure as the previous one, with nodes and edges given by

$$\mathbf{x}_i^{(t+1)} = \left[\mathbf{x}_i^{(0)}, \mathbf{h}_i^{(t+1)} \right] \quad (11)$$

$$\mathbf{x}_{ij}^{(t+1)} = \left[\mathbf{x}_{ij}^{(0)}, \mathbf{h}_{ij}^{(t+1)} \right] \quad (12)$$

where $[\cdot, \cdot]$ denotes concatenation. Including the initial inputs at $t = 0$, referred to as a “skip connection” in ML literature [45], is an important ingredient to capture correlations efficiently and mitigate the vanishing gradient problem. The initial hidden states $\mathbf{h}_i^{(0)}$, $\mathbf{h}_{ij}^{(0)}$ are learnable free parameters which are independent of i and j to

respect permutation equivariance. The construction of the initial feature vectors $\mathbf{x}_i^{(0)}$, $\mathbf{x}_{ij}^{(0)}$ is problem dependent and will be discussed in detail when showing a specific application to the electron gas.

Finally, the backflow-coordinates are constructed as $\mathbf{y}_i(\mathbf{X}) = \mathbf{r}_i + \delta \mathbf{r}_i(\mathbf{X})$. The displacements $\delta \mathbf{r}_i(\mathbf{X})$ are obtained by linearly transforming the node features of the last graph at iteration $t = T$ to d dimensions i.e. $\delta \mathbf{r}_i(\mathbf{X}) = W \cdot \mathbf{x}_i^{(T)}$ with $W \in \mathbb{C}^{d \times D_1}$. The use of complex-valued backflow transformations allows changing the amplitudes of the chosen single-particle orbitals as well as representing complex-valued wave functions in general.

Inspired by the functional form of Eq. (6), we augment the orbitals with a permutation-invariant factor J to yield a variational Ansatz whose functional structure resembles the exact form of Eq. (6):

$$\Psi(\mathbf{X}) = \det\{\varphi_\mu(\mathbf{y}_i(\mathbf{X}))\}. \quad (13)$$

where $\varphi_\mu(\mathbf{y}_i) = \exp[J(\mathbf{Y}, \mu)] \times \phi_\mu(\mathbf{y}_i)$.

C. Electron Gas

We now specialize our discussion on the case of the homogeneous electron gas (HEG) in $d = 3$ spatial dimensions, a prototypical model for the electronic structure in a solid. It includes Coulomb interactions among the solids’ electrons while treating the positively charged ions of the solid as a uniform, static, positive background [46]. Despite these simplifications, the HEG exhibits different phases of matter and captures certain properties of real solids, particularly of Alkali metals. Consider a system consisting of N electrons with an average electron density $n = \frac{N}{V}$. The Hamiltonian (in units of Hartree) is given by:

$$H = -\frac{1}{2r_s^2} \sum_i^N \nabla_{\mathbf{r}_i}^2 + \frac{1}{r_s} \sum_{i < j}^N \frac{1}{\|\mathbf{r}_i - \mathbf{r}_j\|} + \text{const.} \quad (14)$$

where we introduce the Wigner-Seitz radius $r_s = \sqrt[3]{3/(4\pi n)}$ as the characteristic length scale, and a constant arising from the interactions of the electrons with the static, positive background [38]. The conditionally convergent series of the pairwise Coulomb interactions is evaluated using the Ewald summation technique, as is standard in the treatment of extended systems in QMC [47–49]. We assume a fixed spin-polarization with $N = N_\uparrow + N_\downarrow$, where N_\uparrow (N_\downarrow) denotes the number of up/down spins. The spin of electron i is denoted by $s_i \in \{\uparrow, \downarrow\}$. Furthermore, to access the bulk properties of the system, we restrict it to a cubic simulation cell of side length L , equipped with periodic boundary conditions (PBCs) in all spatial directions. For the reference state $\Phi_0(\mathbf{X})$, we consider a mean-field wave function consisting of a single Slater determinant constructed from single-particle orbitals. The choice of orbitals is physically motivated, and for the translation invariant HEG, plane wave

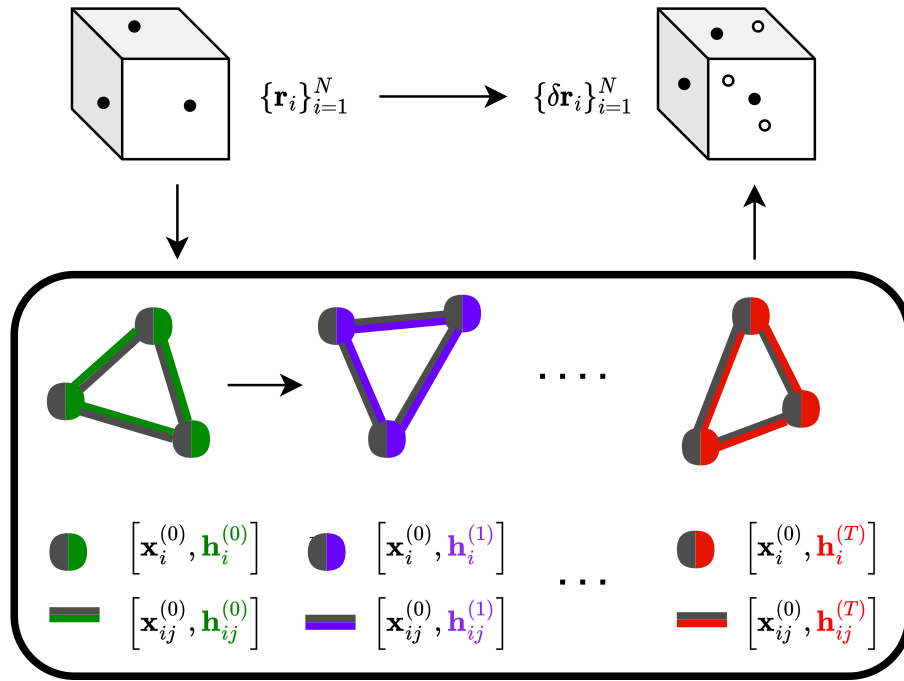


Figure 1. Schematic illustration of the backflow transformation, which transforms single-particle coordinates $\mathbf{r}_i \in \mathbb{R}^d$ (black dots, top left) to quasi-particle coordinates $\delta\mathbf{r}_i \in \mathbb{C}^d$ via the MPNN (black/white dots for real/imaginary part, top right). The MPNN constructs an initial graph that consists of an initial feature vector (dark grey) and a hidden state (green). This graph is then transformed via messages, defined in Eq. 7, to another graph consisting of the initial feature vectors and an updated hidden state (indicated by different coloring). After the final iteration, the node states are linearly transformed to the quasi-particle positions $\delta\mathbf{r}_i = W \cdot \mathbf{h}_i^{(T)}$, which now contain information about all particles (D is the dimension of the last graph’s nodes).

orbitals are a natural choice: $\phi_{\mathbf{k}}(\mathbf{r}) = \exp[i\mathbf{k} \cdot \mathbf{r}]$ with $\mathbf{k} = \frac{2\pi}{L}\mathbf{n}$ where $\mathbf{n} \in \mathbb{Z}^d$. To take into account spin, we use the spin-orbitals $\phi_{\mu}(\mathbf{r}, s) = \phi_{\mathbf{k}_{\mu}}(\mathbf{r})\delta_{s_{\mu}, s}$, where s denotes the spin of the particle at position \mathbf{r} , and each spin-orbital is characterized by the quantum numbers $\mu = (\mathbf{k}_{\mu}, s_{\mu})$. This choice of orbitals allows us to fix the total momentum of the system $\mathbf{k}_{\text{tot}} = \sum_{i=1}^N \mathbf{k}_i$. Furthermore, the choice of orbitals allows us to factorize the determinant into a product of determinants of up and down spin orbitals.

D. MP-NQS for the Electron Gas

To specialize the MP-NQS architecture to the HEG, we only need to define the initial feature vectors. Since the HEG is invariant under continuous translations and spin inversion, we do not input single-particle information (single-particle positions/spins) to the initial node features. Instead, we use a learnable embedding vector $\mathbf{e} \in \mathbb{R}^{D_1}$, that does not depend on the particle index i . For the edge features, we use the translation invariant particle-distances $\mathbf{r}_{ij} = \mathbf{r}_i - \mathbf{r}_j$ and their norm. To distinguish same- and opposite-spin pairs without breaking the spin-inversion symmetry of the problem, we input products of the form $s_i \cdot s_j = \pm 1$ to the edge features.

Overall, we get the following initial feature vectors:

$$\mathbf{x}_i^{(0)} = \mathbf{e} \quad (15)$$

$$\mathbf{x}_{ij}^{(0)} = [\mathbf{r}_{ij}, \|\mathbf{r}_{ij}\|, s_i \cdot s_j]. \quad (16)$$

Notice that with this choice, the resulting backflow coordinate \mathbf{y}_i preserves the spin quantum number s_i of the particle i exactly.

To respect the PBCs of the simulation box, we apply the method introduced in Ref. [21]. The components of a vector $\mathbf{r} \in \mathbb{R}^d$ (where \mathbf{r} can represent a single-particle position vector \mathbf{r}_i or a distance vector \mathbf{r}_{ij}) are mapped to a Fourier basis $\mathbf{r} \mapsto [\sin(\frac{2\pi}{L}\mathbf{r}), \cos(\frac{2\pi}{L}\mathbf{r})] \in \mathbb{R}^{2d}$ and the norm of the distance between two particles $\|\mathbf{r}_{ij}\|$ is replaced with a periodic surrogate $\|\mathbf{r}_{ij}\| \mapsto \|\sin(\frac{\pi}{L}\mathbf{r}_{ij})\|$.

In sum, our Ansatz allows us to fix the total momentum \mathbf{k}_{tot} , while being translation invariant and respecting spin-inversion symmetry. Furthermore, the MP-NQS can change the nodal surface with a number of variational parameters independent of the system size. The variational Ansatz for the HEG uses around ~ 19000 variational parameters and can be trained within $\mathcal{O}(10^3)$ optimization steps while reaching state-of-the-art accuracy. A detailed comparison to other existing NQS approaches is given in Appendix C.

III. RESULTS AND DISCUSSION

We test our variational Ansatz for the fully spin-polarized and unpolarized electron gas, in different density regimes $r_s \in [1, 100]$, and up to system sizes of $N = 128$ electrons. We benchmark our ground-state energies against a variety of methods. For large densities the reference results are obtained using transcorrelation augmented full configuration interaction method (FCI) and distinguishable clusters with doubles (DCD) method [34], both commonly used in quantum chemistry. At low densities, state-of-the-art results are obtained using *Diffusion Monte Carlo* (DMC) with backflow (BF-DMC) [50, 51]. As mentioned above, competitive results from currently available NQS architectures – FermiNet [23] and WAPNet [22] (which uses modified FermiNet-layers) – are available only for small system sizes $N \in \{14, 19\}$. For $N = 128$ electrons, we investigate the low-density regime at $r_s = 110, 200$, and compare to fixed-node DMC (FN-DMC) results, obtained as described in Appendix D.

FN-DMC is also used to assess the effect of our backflow transformation on the nodal surface (dictated by the choice of orbitals) for $N \in \{27, 54\}$ particles. We use an energy of 1 mHa per particle (chemical accuracy) to judge the significance of energy differences between the different methods. A full overview of our results, as well as all benchmarks for the different system sizes and densities, is provided in Tables I, II, III for the spin-unpolarized case, and Tables IV, V for the spin-polarized case (see Appendix E).

A. Small systems

The results for small system sizes $N \in \{14, 19\}$ are depicted in the top panel of Figure 2. For $N = 14$ FCI can be used up to densities of $r_s = 5$ and delivers the lowest available ground-state energy for the HEG. The energy difference between our Ansatz and the FCI results is lower than 1 mHa per particle, though the computational cost of the FCI method scales exponentially with system size. Other NQS architectures perform comparably to the MP-NQS. The unrestricted version of FermiNet performs slightly better ($\mathcal{O}(10^{-5})$ Ha/N) than both the MP-NQS and WAPNet for $r_s \leq 2$, while the MP-NQS and WAPNet improve over FermiNet for $r_s = 5$. The restricted version of FermiNet yields worse ground-state energies than the MP-NQS over all probed densities [23]. For $r_s \geq 5$, where FCI is intractable, we compare our results to the ones obtained with WAPNet and DCD. We find that our architecture slightly outperforms WAPNet for all of the reported densities. Furthermore, both neural-network-based methods outperform the DCD method. Nevertheless, all results lie within a range of 1 mHa per particle. A similar pattern is visible for the slightly larger, polarized case of $N = 19$ particles: the MP-NQS obtains slightly higher energies

than WAPNet for large densities ($r_s \leq 5$) and slightly lower ones at smaller densities ($r_s \geq 5$). The differences are lower than 1 mHa per particle in all cases and can be considered negligible.

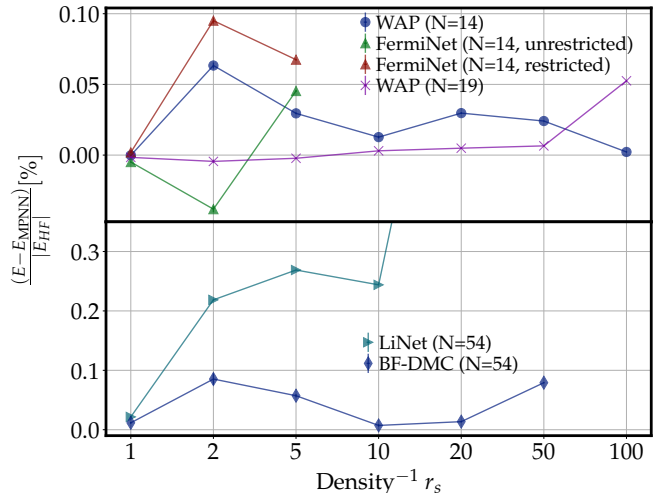


Figure 2. Energy differences between ground-state energies obtained with other methods and with our model relative to the corresponding Hartree Fock energy in the thermodynamic limit for various densities, polarizations, and system sizes. (Top panel) $N = 14, 19$, (Bottom panel): $N = 54$ particles. Error bars are too small to be visible for most densities. The corresponding numerical data can be found in Appendix E.

B. Large systems

For the larger system size of $N = 54$ particles, we can only compare with FCI at high density $r_s = 1$, where our method achieves the same level of accuracy. As the system size increases, the difference between our results and FCI decreases, with the two methods yielding statistically indistinguishable results for $N = 54$.

We obtain significantly better ground-state energies than BF-DMC, especially at high densities. This is in stark contrast to the (FermiNet-based) architecture of [27] (dubbed LiNet in the following), which does not improve upon BF-DMC energies over the whole density regime (see Figure 2, bottom panel). Comparison to DCD data shows that the MP-NQS can consistently improve the ground-state energies for all examined densities, with energy differences exceeding 1 mHa per particle. This indicates that while the accuracy of DCD decreases with increasing system size, our method appears to maintain its accuracy independent of system size. As expected, we reach higher accuracy compared to FN-DMC due to the optimization of the nodal surface. The difference is ~ 1 mHa per particle at the largest density but decreases with decreasing density because the nodal surface does not contribute as much to the ground-state energy in this regime. Similar behavior is seen for the

BF-DMC results on the same system size as well as for the FN-DMC results on $N = 27$ particles. The results on the $N = 54$ unpolarized system exemplify the accuracy of our variational Ansatz, which does not depend significantly on the system size or density.

C. Wigner Crystallization

A phase transition from liquid to crystalline phase is expected for the HEG, as a function of the density n . The dominating kinetic energy in Eq. (14) ($\sim 1/r_s^2$) for large n , leads to the well-known Fermi liquid behavior. Contrary for small n , the potential energy ($\sim 1/r_s$) dominates and enforces a crystalline structure among the electrons known as the Wigner crystal. The Wigner crystal, expected to be of BCC type [52], is translation invariant, and the resulting crystal structure is therefore called a *floating* crystal. The latter is characterized by a homogeneous single-particle density distribution and a crystalline two-body radial distribution function.

In previous QMC simulations of the Wigner crystal phase (e.g. in the works of Refs. [23, 35, 53]), the transition is investigated using a variational Ansatz that explicitly breaks translation symmetry. As a result, these works find a pinned BCC lattice rather than the translation invariant version. The pinned crystal is additionally induced by using Gaussian orbitals centered around BCC lattice sites, a primitive BCC simulation cell, or both. Detection of the translation invariant transition, without any biasing towards a BCC structure, has not been realized up to now, to the best of our knowledge.

We use here the MP-NQS as an unbiased, translation invariant variational Ansatz to investigate the transition in a conventional BCC cell i.e. a simple cubic simulation cell. We study system sizes of $N = 54, 128$ particles at $r_s = 5, 110, 200$. The resulting radial distribution functions for $N = 54, 128$ particles are displayed in Figure 3, 4, respectively. At high densities ($r_s = 5$), we obtain typical Fermi liquid behavior. Interactions cause the $g_2(r)$ exchange hole to drop from 0.5 predicted by Hartree-Fock, to below 0.1. No correlations are found between particles at large distances (indicated by $g_2(r) = 1$). With decreasing density ($r_s = 110$), the finite $g_2(0)$ vanishes, as the potential energy forces particles apart. For $r_s = 110$ and $N = 54$ particles, we observe a slight departure of the radial distribution w.r.t. an unpolarized fluid in the first maximum [53]. For larger distances, we again reproduce the fluid benchmark. While this could be seen as the formation of a crystalline structure, scaling to a larger system size of $N = 128$ particles reveals a finite size effect as putative long-range correlations decay rapidly for increasing distances. The FN-DMC results also support this finding. We therefore conclude that we do not observe the translation invariant Wigner crystal phase at $r_s = 110$. For even lower densities ($r_s = 200$) we observe increasing oscillations up to larger distances. Compared to radial distribution functions obtained using

(translation invariance breaking) Gaussian orbitals, the oscillations that we observe decay slightly faster.

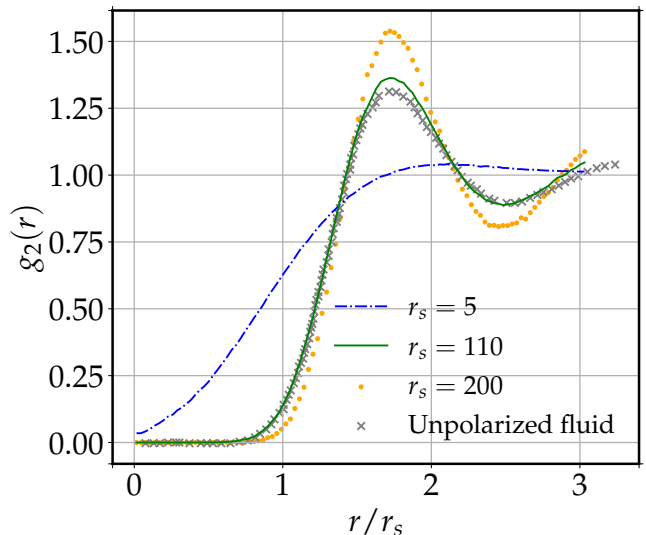


Figure 3. Spin-averaged radial distribution function for the HEG system with $N = 54$ particles at low densities ($r_s = 5, 110, 200$). The error bars are smaller than the symbols. The unpolarized fluid is obtained from [53] for $r_s = 110$.

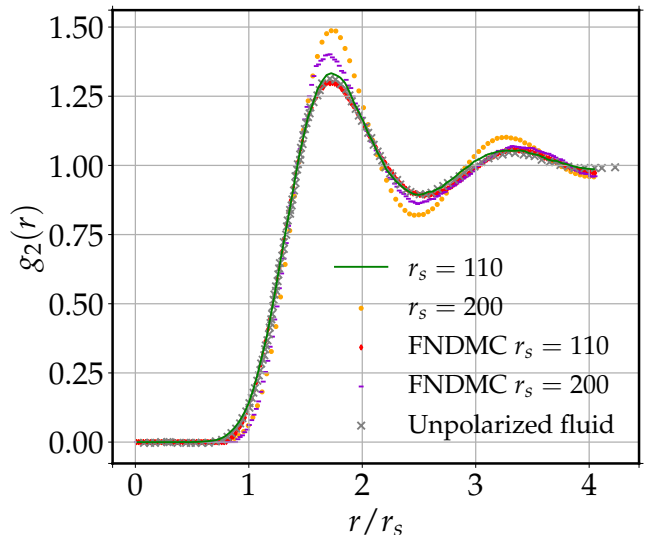


Figure 4. Spin-averaged radial distribution function for the HEG system with $N = 128$ particles at low densities ($r_s = 110, 200$). The error bars are smaller than the symbols. The unpolarized fluid is obtained from [53] for $r_s = 110$.

IV. CONCLUSIONS

We have introduced a novel NQS architecture that uses message-passing neural networks to build highly corre-

lated backflow coordinates, which accurately represent fermionic many-body quantum states. We demonstrate its power on the HEG system, showing that our model decreases the number of parameters by orders of magnitudes compared to other state-of-the-art NQS in continuous space. We also demonstrate that by simplifying the model complexity, we can take advantage of powerful higher-order optimization techniques such as stochastic reconfiguration [31], which can reduce the number of necessary optimization steps by two orders of magnitude. The favourable scaling allows us to accurately simulate large system sizes, previously inaccessible to all other state-of-the-art NQS models. We are able to increase the available system sizes from $N = 27$ and $N = 54$ particles in periodic systems [22, 23, 27] and $N = 72$ particles for molecular systems [43] to $N = 128$ particles in this work. We reach at par accuracy for small system sizes, where NQS results are available, and outperform state-of-the-art backflow-DMC results on larger system sizes. This leads us to conclude that our architecture and optimization scheme constitutes a significant improvement over existing methods. We hence open the door to extrapolation methods to the thermodynamic limit for extended systems.

Using an unbiased simulation cell and a translation invariant Ansatz, we do not observe a crystallization for $N = 54, 128$ particles for densities $r_s \leq 110$. We leave to further investigation the problem of resolving the tension with existing predictions [35, 53] on the location of the

phase transition.

In addition to the numerical results, we have also introduced an analytical argument to justify the commonly adopted backflow transformations. Our argument shows that, at least in principle, a backflow transformation over a reference state is enough to obtain the exact ground-state wave function. It will be especially interesting to characterize the geometrical properties of these transformations, to understand in what cases neural-network parameterizations can effectively describe them.

ACKNOWLEDGEMENTS

Stimulating discussions with Markus Holzmann, and Francesco Pederiva are gratefully acknowledged. The numerical tools used in this work are based on the open-source software NetKet[54–56] version 3.0. The present research is supported by the Swiss National Science Foundation under Grant No. 200021_200336, Microsoft Research, by the U.S. Department of Energy, Office of Science, Office of Nuclear Physics, under contracts DE-AC02-06CH11357 (A.L.), by the 2020 DOE Early Career Award program (A.L.), the NUCLEI SciDAC program (A.L.), and Argonne LDRD awards (A. L.). J. K. is supported by the U.S. Department of Energy, Office of Science, office of Nuclear Physics under grant No. DE-SC0021152 and U.S. National Science Foundation Grants No. PHY-1404159 and PHY-2013047.

-
- [1] B. M. Austin, D. Y. Zubarev, and W. A. Lester Jr, Quantum monte carlo and related approaches, *Chemical reviews* **112**, 263 (2012).
 - [2] J. Carlson, S. Gandolfi, F. Pederiva, S. C. Pieper, R. Schiavilla, K. Schmidt, and R. B. Wiringa, Quantum monte carlo methods for nuclear physics, *Reviews of Modern Physics* **87**, 1067 (2015).
 - [3] A. J. Leggett, A theoretical description of the new phases of liquid ^3He , *Rev. Mod. Phys.* **47**, 331 (1975).
 - [4] M. Tinkham, *Introduction to superconductivity* (Courier Corporation, 2004).
 - [5] G. Carleo and M. Troyer, Solving the quantum many-body problem with artificial neural networks, *Science* **355**, 602 (2017).
 - [6] J. Carrasquilla, Machine learning for quantum matter, *Advances in Physics: X* **5**, 1797528 (2020).
 - [7] K. Choo, G. Carleo, N. Regnault, and T. Neupert, Symmetries and many-body excitations with neural-network quantum states, *Phys. Rev. Lett.* **121**, 167204 (2018).
 - [8] F. Ferrari, F. Becca, and J. Carrasquilla, Neural gutzwiller-projected variational wave functions, *Phys. Rev. B* **100**, 125131 (2019).
 - [9] M. Hibat-Allah, M. Ganahl, L. E. Hayward, R. G. Melko, and J. Carrasquilla, Recurrent neural network wave functions, *Phys. Rev. Res.* **2**, 023358 (2020).
 - [10] M. Bukov, M. Schmitt, and M. Dupont, Learning the ground state of a non-stoquastic quantum Hamiltonian in a rugged neural network landscape, *SciPost Phys.* **10**, 147 (2021).
 - [11] Y. Nomura and M. Imada, Dirac-type nodal spin liquid revealed by refined quantum many-body solver using neural-network wave function, correlation ratio, and level spectroscopy, *Phys. Rev. X* **11**, 031034 (2021).
 - [12] N. Astrakhantsev, T. Westerhout, A. Tiwari, K. Choo, A. Chen, M. H. Fischer, G. Carleo, and T. Neupert, Broken-symmetry ground states of the heisenberg model on the pyrochlore lattice, *Phys. Rev. X* **11**, 041021 (2021).
 - [13] D.-L. Deng, X. Li, and S. D. Sarma, Quantum entanglement in neural network states, *Physical Review X* **7**, 021021 (2017).
 - [14] Y. Levine, O. Sharir, N. Cohen, and A. Shashua, Quantum entanglement in deep learning architectures, *Phys. Rev. Lett.* **122**, 065301 (2019).
 - [15] D. Luo and B. K. Clark, Backflow transformations via neural networks for quantum many-body wave functions, *Phys. Rev. Lett.* **122**, 226401 (2019).
 - [16] K. Choo, A. Mezzacapo, and G. Carleo, Fermionic neural-network states for ab-initio electronic structure, *Nature communications* **11**, 1 (2020).
 - [17] J. Robledo Moreno, G. Carleo, A. Georges, and J. Stokes, Fermionic wave functions from neural-network constrained hidden states, *Proceedings of the National Academy of Sciences* **119**, e2122059119 (2022).

- [18] D. Pfau, J. S. Spencer, A. G. D. G. Matthews, and W. M. C. Foulkes, Ab initio solution of the many-electron schrödinger equation with deep neural networks, *Phys. Rev. Res.* **2**, 033429 (2020).
- [19] J. Hermann, Z. Schätzle, and F. Noé, Deep-neural-network solution of the electronic schrödinger equation, *Nature Chemistry* **12**, 891 (2020).
- [20] M. Entwistle, Z. Schätzle, P. A. Erdman, J. Hermann, and F. Noé, Electronic excited states in deep variational monte carlo, *Nature Communications* **14**, 274 (2023).
- [21] G. Pescia, J. Han, A. Lovato, J. Lu, and G. Carleo, Neural-network quantum states for periodic systems in continuous space, *Physical Review Research* **4**, 023138 (2022).
- [22] M. Wilson, S. Moroni, M. Holzmann, N. Gao, F. Wudarski, T. Vegge, and A. Bhowmik, Wave function ansatz (but periodic) networks and the homogeneous electron gas, arXiv preprint arXiv:2202.04622 (2022).
- [23] G. Cassella, H. Sutterud, S. Azadi, N. D. Drummond, D. Pfau, J. S. Spencer, and W. M. C. Foulkes, Discovering quantum phase transitions with fermionic neural networks, *Phys. Rev. Lett.* **130**, 036401 (2023).
- [24] C. Adams, G. Carleo, A. Lovato, and N. Rocco, Variational monte carlo calculations of $a \leq 4$ nuclei with an artificial neural-network correlator ansatz, *Phys. Rev. Lett.* **127**, 022502 (2021).
- [25] A. Gnech, C. Adams, N. Brawand, G. Carleo, A. Lovato, and N. Rocco, Nuclei with up to $\{A=6\}a=6$ nucleons with artificial neural network wave functions, *Few-Body Systems* **63**, 1 (2022).
- [26] A. Lovato, C. Adams, G. Carleo, and N. Rocco, Hidden-nucleons neural-network quantum states for the nuclear many-body problem, *Physical Review Research* **4**, 043178 (2022).
- [27] X. Li, Z. Li, and J. Chen, Ab initio calculation of real solids via neural network ansatz, *Nature Communications* **13**, 7895 (2022).
- [28] H. Xie, L. Zhang, and L. Wang, m^* of two-dimensional electron gas: a neural canonical transformation study (2022), arXiv:2201.03156 [cond-mat, physics:physics].
- [29] B. Fore, J. M. Kim, G. Carleo, M. Hjorth-Jensen, and A. Lovato, Dilute neutron star matter from neural-network quantum states, arXiv preprint arXiv:2212.04436 (2022).
- [30] J. Toulouse and C. J. Umrigar, Optimization of quantum Monte Carlo wave functions by energy minimization, *J. Chem. Phys.* **126**, 084102 (2007), arXiv:physics/0701039 [physics.chem-ph].
- [31] S. Sorella, Green function monte carlo with stochastic reconfiguration, *Phys. Rev. Lett.* **80**, 4558 (1998).
- [32] C. Lin, F. Zong, and D. M. Ceperley, Twist-averaged boundary conditions in continuum quantum monte carlo algorithms, *Physical Review E* **64**, 016702 (2001).
- [33] N. Drummond and R. Needs, Diffusion quantum monte carlo calculation of the quasiparticle effective mass of the two-dimensional homogeneous electron gas, *Physical Review B* **87**, 045131 (2013).
- [34] K. Liao, T. Schraivogel, H. Luo, D. Kats, and A. Alavi, Towards efficient and accurate ab initio solutions to periodic systems via transcorrelation and coupled cluster theory, *Phys. Rev. Research* **3**, 033072 (2021).
- [35] S. Azadi, N. Drummond, and S. Vinko, Correlation energy of the paramagnetic electron gas at the thermodynamic limit, arXiv preprint arXiv:2209.10227 (2022).
- [36] J. Gilmer, S. S. Schoenholz, P. F. Riley, O. Vinyals, and G. E. Dahl, Neural message passing for quantum chemistry, in *International conference on machine learning* (PMLR, 2017) pp. 1263–1272.
- [37] R. P. Feynman and M. Cohen, Energy spectrum of the excitations in liquid helium, *Phys. Rev.* **102**, 1189 (1956).
- [38] Y. Kwon, D. M. Ceperley, and R. M. Martin, Effects of backflow correlation in the three-dimensional electron gas: Quantum monte carlo study, *Phys. Rev. B* **58**, 6800 (1998).
- [39] Y. Kwon, D. Ceperley, and R. M. Martin, Effects of three-body and backflow correlations in the two-dimensional electron gas, *Physical Review B* **48**, 12037 (1993).
- [40] M. Ruggeri, S. Moroni, and M. Holzmann, Nonlinear network description for many-body quantum systems in continuous space, *Phys. Rev. Lett.* **120**, 205302 (2018).
- [41] M. Taddei, M. Ruggeri, S. Moroni, and M. Holzmann, Iterative backflow renormalization procedure for many-body ground-state wave functions of strongly interacting normal fermi liquids, *Physical Review B* **91**, 115106 (2015).
- [42] A. Vaswani, N. Shazeer, N. Parmar, J. Uszkoreit, L. Jones, A. N. Gomez, L. Kaiser, and I. Polosukhin, Attention is all you need, *Advances in neural information processing systems* **30** (2017).
- [43] I. von Glehn, J. S. Spencer, and D. Pfau, A self-attention ansatz for ab-initio quantum chemistry, arXiv preprint arXiv:2211.13672 (2022).
- [44] D. Hendrycks and K. Gimpel, Gaussian error linear units (gelus), arXiv preprint arXiv:1606.08415 (2016).
- [45] K. He, X. Zhang, S. Ren, and J. Sun, Deep residual learning for image recognition, in *Proceedings of the IEEE conference on computer vision and pattern recognition* (2016) pp. 770–778.
- [46] D. Pines, *Elementary excitations in solids*, edited by jd jackson and d. pines (1963).
- [47] P. P. Ewald, Die berechnung optischer und elektrostatischer gitterpotentiale, *Annalen der physik* **369**, 253 (1921).
- [48] L. M. Fraser, W. M. C. Foulkes, G. Rajagopal, R. J. Needs, S. D. Kenny, and A. J. Williamson, Finite-size effects and coulomb interactions in quantum monte carlo calculations for homogeneous systems with periodic boundary conditions, *Phys. Rev. B* **53**, 1814 (1996).
- [49] A. Y. Toukmaji and J. A. Board Jr, Ewald summation techniques in perspective: a survey, *Computer physics communications* **95**, 73 (1996).
- [50] P. López Ríos, A. Ma, N. D. Drummond, M. D. Towler, and R. J. Needs, Inhomogeneous backflow transformations in quantum monte carlo calculations, *Phys. Rev. E* **74**, 066701 (2006).
- [51] S. Azadi and N. D. Drummond, Low-density phase diagram of the three-dimensional electron gas, *Phys. Rev. B* **105**, 245135 (2022).
- [52] E. Wigner, On the interaction of electrons in metals, *Phys. Rev.* **46**, 1002 (1934).
- [53] N. Drummond, Z. Radnai, J. Trail, M. Towler, and R. Needs, Diffusion quantum monte carlo study of three-dimensional wigner crystals, *Physical Review B* **69**, 085116 (2004).
- [54] G. Carleo, K. Choo, D. Hofmann, J. E. Smith, T. Westerhout, F. Alet, E. J. Davis, S. Efthymiou, I. Glasser, S.-H. Lin, *et al.*, Netket: a machine learning toolkit for many-

- body quantum systems, *SoftwareX* **10**, 100311 (2019).
- [55] D. Häfner and F. Vicentini, mpi4jax: Zero-copy mpi communication of jax arrays, *Journal of Open Source Software* **6**, 3419 (2021).
- [56] F. Vicentini, D. Hofmann, A. Szabó, D. Wu, C. Roth, C. Giuliani, G. Pescia, J. Nys, V. Vargas-Calderón, N. Astrakhantsev, *et al.*, Netket 3: Machine learning toolbox for many-body quantum systems, *SciPost Physics Codebases*, 007 (2022).
- [57] E. Neuscamman, C. J. Umrigar, and G. K.-L. Chan, Optimizing large parameter sets in variational quantum monte carlo, *Phys. Rev. B* **85**, 045103 (2012).
- [58] T. M. Whitehead, M. H. Michael, and G. J. Conduit, Jastrow correlation factor for periodic systems, *Phys. Rev. B* **94**, 035157 (2016), [arXiv:1607.05921 \[cond-mat.str-el\]](https://arxiv.org/abs/1607.05921).
- [59] B. S. Pudliner, V. R. Pandharipande, J. Carlson, S. C. Pieper, and R. B. Wiringa, Quantum Monte Carlo calculations of nuclei with $A \leq 7$, *Phys. Rev. C* **56**, 1720 (1997), [arXiv:nucl-th/9705009](https://arxiv.org/abs/nucl-th/9705009).
- [60] S. Gandolfi, D. Lonardonì, A. Lovato, and M. Piarulli, Atomic nuclei from quantum Monte Carlo calculations with chiral EFT interactions, *Front. in Phys.* **8**, 117 (2020), [arXiv:2001.01374 \[nucl-th\]](https://arxiv.org/abs/2001.01374).

Appendix A: Optimization

From the Rayleigh-Ritz principle, we obtain a lower bound on the expectation value of the Hamiltonian $\langle \Psi | H | \Psi \rangle / \langle \Psi | \Psi \rangle \equiv E[\Psi] \geq E_0$. We use the energy expectation value with respect to our variational Ansatz as a cost function to gauge the proximity of the variational state to the ground state of the Hamiltonian. Formally the ground state is given by:

$$\Psi_0 = \arg \min_{\Psi} E[\Psi]. \quad (\text{A1})$$

where $H |\Psi_0\rangle = E_0 |\Psi_0\rangle$.

Since the exact expected value of the Hamiltonian requires us to analytically solve a high-dimensional integral, which in general is not feasible, we resort to Monte Carlo sampling and integration. The energy expectation is evaluated as the average over a set of local energy $E_{\text{loc}}(\mathbf{X}) = \langle \mathbf{X} | H | \Psi \rangle / \langle \mathbf{X} | \Psi \rangle$, where the samples \mathbf{X} are obtained from the probability distribution $|\Psi(\mathbf{X})|^2 / \langle \Psi | \Psi \rangle$ using the Metropolis-Hastings algorithm.

To update the variational parameters in our Ansatz such that it exhibits progressively lower energy expectation values, we apply the stochastic reconfiguration (SR) algorithm [31], which can be shown to be equivalent to imaginary-time evolution on the variational manifold and is related to the Natural Gradient descent method. The update rule for the variational parameters is given by $\delta \boldsymbol{\theta} = -\eta S^{-1} \mathbf{F}$, where \mathbf{F} is the force vector consisting of the log-derivatives of the energy w.r.t. the variational parameters $\boldsymbol{\theta}$ given by

$$F_i = 2 \left(\frac{\langle \partial_i \Psi | H | \Psi \rangle}{\langle \Psi | \Psi \rangle} - E[\Psi] \frac{\langle \partial_i \Psi | \Psi \rangle}{\langle \Psi | \Psi \rangle} \right), \quad (\text{A2})$$

and the so-called quantum geometric tensor S is

$$S_{ij} = \frac{\langle \partial_i \Psi | \partial_j \Psi \rangle}{\langle \Psi | \Psi \rangle} - \frac{\langle \partial_i \Psi | \Psi \rangle \langle \Psi | \partial_j \Psi \rangle}{\langle \Psi | \Psi \rangle \langle \Psi | \Psi \rangle}, \quad (\text{A3})$$

and η is the learning rate [57]. To regularize the computation of S^{-1} , we apply a small diagonal shift such that we actually compute $(S + \epsilon \mathbb{I})^{-1}$. For all experiments, we used $\epsilon = 10^{-4}$. The learning rate was chosen dependent on the density as $\eta = \{0.05, 0.05, 0.05, 0.1, 0.1, 0.5, 1, 2.5\}$ for $r_s = \{1, 2, 5, 10, 20, 50, 100, 110\}$.

Appendix B: MP-NQS

We show in Figure 5, for a system of $N = 14$ particles at the largest densities $r_s = 1, 2, 5$, that increasing the number of backflow iterations (and therefore the number of variational parameters) systematically improves our Ansatz’s accuracy. At $r_s = 1$ we score slightly worse than WAPNet for a single backflow iteration, while reaching the same accuracy for three backflow iterations. Similarly, for $r_s = 2$ we obtain a slightly higher energy than WAPNet for a single backflow iteration, but we surpass WAPNet’s performance after two backflow iterations. For $r_s = 5$ we obtain more precise results than WAPNet for a single backflow iteration. Upon comparison to FermiNet, our results demonstrate that we consistently outperform the unrestricted, single Slater determinant version of FermiNet at these densities. Interestingly, for lower densities ($r_s = 5$), our Ansatz with a single message-passing iteration outperforms even the unrestricted FermiNet with 16 determinants.

Appendix C: Comparison to other NQS architectures

The most thoroughly investigated NQS architectures for continuous space are FermiNet and PauliNet [18, 19]. Both have been shown to provide good approximations to the ground-state energies of molecular systems. FermiNet has additionally been applied to the HEG system with very accurate results [23]. Although FermiNet shows slightly better results on molecular systems than PauliNet, differences in the architectures allow PauliNet to reach comparable energies with considerably less parameters than FermiNet. Here we compare our MP-NQS to these two Ansatzes and highlight similarities and differences.

Both FermiNet and PauliNet construct the variational wave function Ansatz by using the antisymmetry of the Slater determinant. PauliNet uses physically motivated orbital functions as input to the Slater determinant and alters these by an orbital-aware multiplicative symmetric factor. Additionally, an overall Jastrow factor is used to increase the expressiveness of the Ansatz. FermiNet imposes no physical knowledge on the orbitals (up to an

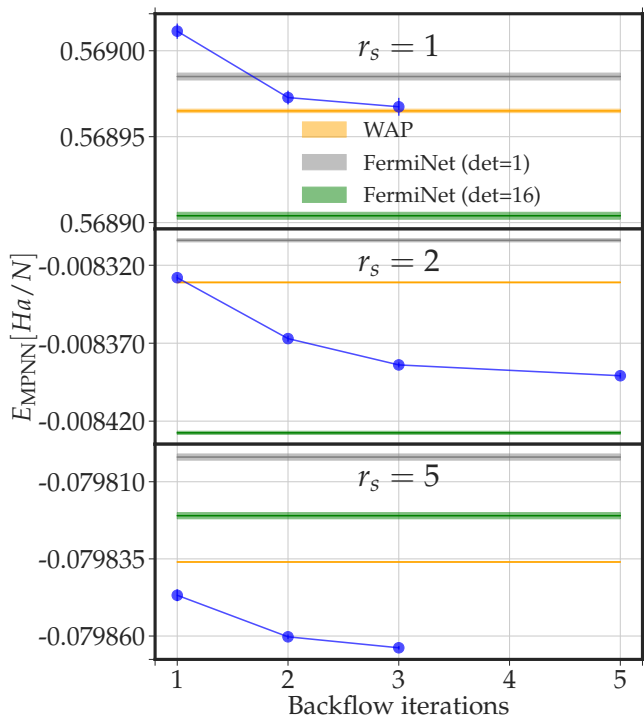


Figure 5. Energy obtained with our variational Ansatz for $N = 14$ particles at the densities $r_s = 1, 2, 5$ as a function of the number of message-passing backflow iterations. We compare to WAPNet and FermiNet with a single Slater determinant as well as FermiNet with 16 determinants.

overall envelope function) and does not need an overall Jastrow factor. To construct the multiplicative factor in PauliNet and the orbitals in FermiNet, the number of parameters scales linearly with the system size. In addition, both Ansatzes construct multiple Slater determinants to increase their accuracy, thereby multiplying the number of parameters by a constant factor. Both Ansatzes treat the different spin species by utilizing distinct parameter sets for the different possible spin projections.

Similar to PauliNet, we use physically motivated orbitals which are evaluated at backflowed coordinates. The latter are constructed by using a novel and powerful MPNN that leverages the expressiveness of the attention mechanism. There exists yet another version of FermiNet, called PsiFormer, that uses the original self-attention mechanism introduced in [42], but has not been applied to extended systems. While PsiFormer applies the attention mechanism along the *feature dimension* of the single-particle stream, we find substantially improved results by applying attention along the *particle dimension* instead. This approach introduces additional correlations between the particles rather than between the features of the edge-states of our graphs. As PauliNet, we use a multiplicative factor to alter the orbitals even further, which allows us to omit the overall Jastrow factor that is present in PauliNet. By inputting orbital information to the multiplicative factor directly, we can keep

the number of parameters independent of the number of particles. Notably, our Ansatz does not require multiple Slater-determinants.

As mentioned above, FermiNet has been applied to study the HEG in continuous space. The orbitals are constructed from scratch with plane-wave envelope functions. In contrast to our approach, FermiNet uses large networks (512 width) to process the positions of the simulated particles and considerably smaller networks (32 width) to act on the distance vectors between the particles. The usage of single-particle coordinates breaks the translation invariance of the system. In our MPNN, we only use the distance information between the particles and ignore the single-particle information in order to stay translation invariant. We only use small networks (32 width) to construct the messages $m_{ij}^{(t+1)}$ (Eq. 7) that are used to update the nodes and edges of the particle graph.

Overall, we use around 19000 parameters in our Ansatz which consists of a single Slater determinant. PauliNet usually uses 70000-100000 parameters and up to 36 Slater determinants, while FermiNet uses on the order of a million parameters with up to 32 Slater determinants. The fact that we have considerably fewer parameters allows us to use SR to optimize our variational Ansatz (see Appendix A). Both FermiNet and PauliNet use $\mathcal{O}(10^5)$ optimization steps, but we can reduce this number to less than $\mathcal{O}(10^3)$ iterations. To illustrate this point, we show the optimization curve for $N = 14$ particles at $r_s = 5$ in Figure 6.

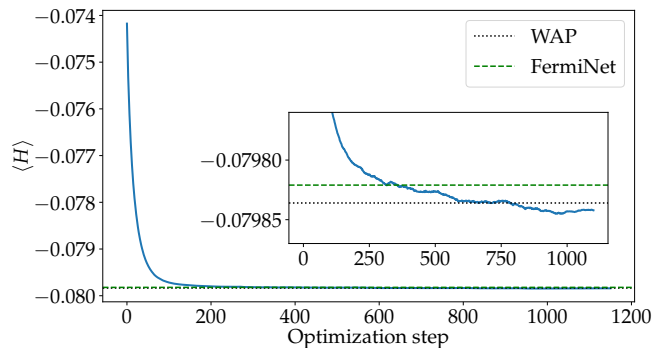


Figure 6. Moving average of the optimization curve (energy per particle in Hartree averaged over 100 optimization iterations) for $N = 14$ particles at $r_s = 5$ obtained with a learning rate $\eta = 0.05$ and a diagonal shift $\epsilon = 10^{-4}$ for SR. We compare to results from WAP-net [22] and FermiNet [23] to our MPNN. Note that the physical motivation orbitals used in our Ansatz makes us start close to the ground-state energy with our optimization.

Appendix D: Diffusion Monte Carlo

The diffusion Monte Carlo (DMC) method projects the variational states $|\Psi_V\rangle$ in imaginary time to filter out its

ground-state component

$$|\Psi_0\rangle \propto \lim_{\tau \rightarrow \infty} e^{-H\tau} |\Psi_V\rangle. \quad (\text{D1})$$

The variational state is taken to be of the Slater-Jastrow form $\Psi_V = e^{J(\mathbf{X})} S_\uparrow S_\downarrow$, where S_\uparrow and S_\downarrow are the Slater determinants of single-electron states for the spin-up and spin-down species, respectively. The Jastrow factor captures correlation between electrons, and hence is a function of electron-electron separation coordinates $\mathbf{r}_{ij} = \{x_{ij}, y_{ij}, z_{ij}\}$

$$J(\mathbf{X}) = \sum_{\substack{i < j \\ \sigma, \tau \in \{\uparrow, \downarrow\}}} J_{\sigma\tau}(\mathbf{r}_{ij}). \quad (\text{D2})$$

The Pauli principle requires the functional form of $J_{\sigma\tau}$ must be even under exchange of particles i and j . In addition, $J_{\sigma\tau}$ must satisfy the periodic-boundary conditions at the edge of the simulation box. To fulfill the above requirements, we utilize the parametrization introduced in Ref. [58]

$$J_{\sigma,\tau}(\mathbf{r}_{ij}) = \sum_{n=1}^{N_j} c_{n,\sigma\tau} [j(x_{ij})^2 + j(y_{ij})^2 + j(z_{ij})^2]^{n/2}, \quad (\text{D3})$$

where $j(x) = |x|[1 - 2(|x|/L)^3]$. By taking $c_{1,\uparrow\uparrow} = c_{1,\downarrow\downarrow} = \frac{1}{4}$ and $c_{1,\uparrow\downarrow} = c_{1,\downarrow\uparrow} = \frac{1}{2}$, the Kato cusp conditions at particle coalescence is also automatically fulfilled. The parameters $c_{n>1,\uparrow\uparrow}$ are determined by minimizing the energy of the systems by using the ‘‘linear’’ optimization scheme [30]. We find that using more than $N_J = 6$ variational parameters does not improve the energy noticeably.

The imaginary-time diffusion is broken into many small steps $\delta\tau$. The Trotter-Suzuki decomposition can be applied to the short-time propagator as $e^{-H\delta\tau} \simeq e^{-V\delta\tau/2} e^{-T\delta\tau} e^{-V\delta\tau/2}$, where T and V are the kinetic and potential energy operators, respectively. At each imaginary-time step, we use the free propagator

$$\begin{aligned} G_0(\mathbf{X}', \mathbf{X}) &\equiv \langle \mathbf{X}' | e^{-T\delta\tau} | \mathbf{X} \rangle \\ &= \left[\sqrt{\frac{m}{2\pi\hbar^2\delta\tau}} \right]^{3N} \exp \left[-\frac{(\mathbf{R}' - \mathbf{R})^2}{2\hbar^2 \delta\tau/m} \right] \end{aligned} \quad (\text{D4})$$

to sample the new coordinates \mathbf{X}' of all particles. As routinely done in nuclear-physics applications [59, 60], to remove the linear terms coming from the exponential of Eq. (D4), we use two mirror samples $\mathbf{X}' = \mathbf{X} \pm \delta\mathbf{X}$, and we consider the corresponding importance-sampled weights

$$w_\pm = \frac{\Psi_V(\mathbf{X} \pm \delta\mathbf{X})}{\Psi_V(\mathbf{X})} e^{-[V(\mathbf{X} \pm \delta\mathbf{X}) + V(\mathbf{X})]\delta\tau/2}. \quad (\text{D5})$$

Only one of the two samples is kept in the propagation according to a heat-bath sampling among the two normalized weights $w_\pm / (\sum_\pm w_\pm)$ and the average weight $\sum_\pm w_\pm / 2$ is assigned to the propagated configuration.

The fermion-sign problem is controlled by employing the fixed-node approximation, which amounts to evaluating the weights of Eq. (D5) with the replacement

$$\frac{\Psi_V(\mathbf{X} \pm \delta\mathbf{X})}{\Psi_V(\mathbf{X})} \rightarrow \text{Re} \left\{ \frac{\Psi_V(\mathbf{X} \pm \delta\mathbf{X})}{\Psi_V(\mathbf{X})} \right\}. \quad (\text{D6})$$

Note that if the real part of the above ratio is negative, the weight of the configuration is set to zero only after computing the average weight.

Appendix E: Results

In Tables I, II, IV and V we show the ground-state energies of the unpolarized and fully polarized HEG for different system sizes $N = \{14, 19, 27, 54\}$ and densities $r_s = \{1, 2, 5, 10, 20, 30, 50, 70, 90, 100\}$.

N	r_s	MP-NQS	WAP [22]	FermiNet [23]	FCI*/DCD** [34]
14	1	0.568967(6)	0.568965(1)	0.568904(1)	0.56861(1)*
	2	-0.008391(1)	-0.0083310(3)	-0.008427(1)	-0.00868(2)*
	5	-0.0798544(4)	-0.0798360(1)	-0.079821(1)	-0.08002(2)*
	10	-0.0552126(6)	-0.05520380(3)	N/A	-0.05509**
	20	-0.0324553(2)	-0.0324434(1)	N/A	-0.03201**
	50	-0.01462631(6)	-0.01462211(4)	N/A	-0.01384**
	100	-0.00773018(3)	-0.007729980(2)	N/A	N/A

Table I. Total energy per particle in Hartree for unpolarized system of $N = 14$ particles. WAPNet and FermiNet are alternative NQS architectures optimized via VMC. We include FCI and DCD results as benchmarks from quantum chemistry.

N	r_s	MP-NQS	LiNet [27]	FN-DMC	BF-DMC [50, 51]	FCI*/DCD** [34]
54	1	0.52973(1)	0.530019(1)	0.53094(2)	0.52989(4)	0.52973(3)*
	2	-0.014046(8)	-0.013840(1)	-0.01326(2)	-0.013966(2)	-0.01379**
	5	-0.079090(2)	-0.0788354(2)	-0.07867(1)	-0.079036(3)	-0.07837**
	10	-0.054448(1)	-0.0542785(1)	-0.054269(8)	-0.054443(2)	-0.05322**
	20	-0.0320524(5)	-0.0316886(1)	-0.031976(8)	-0.032047(2)	-0.03113**
	50	-0.0145015(1)	N/A	-0.01387(2)	-0.0144877(1)	-0.01281**
	100	-0.0076793(1)	N/A	-0.007674(3)	N/A	N/A

Table II. Total energy per particle in Hartree for the unpolarized system of $N = 54$ particles. FN-DMC results are obtained using the method in Appendix D. We include FCI and DCD results as benchmarks from quantum chemistry.

N	r_s	MP-NQS	FN-DMC
128	110	-0.00700711(1)	-0.00677(1)
	200	-0.0040023(2)	-0.0039923(7)

Table III. Total energy per particle in Hartree for the unpolarized system of $N = 128$ particles. FN-DMC results are obtained using the method in Appendix D.

N	r_s	MP-NQS	WAP [22]
19	1	1.046262(2)	1.046241(3)
	2	0.096307(1)	0.096303(1)
	5	-0.0672489(3)	-0.06725105(3)
	10	-0.0528624(2)	-0.05286035(1)
	20	-0.0320101(1)	-0.0320082(1)
	50	-0.01456685(3)	-0.01456571(2)
	100	-0.00771832(2)	-0.00771362(2)

Table IV. Total energy per particle in Hartree for the polarized system of $N = 19$ particles. We compare to results obtained using WAPNet.

N	r_s	MP-NQS	FN-DMC
27	1	1.051771(4)	1.05200(3)
	2	0.098460(2)	0.09866(2)
	5	-0.0665523(6)	-0.066429(4)
	10	-0.0526015(2)	-0.052540(6)
	30	-0.0228184(1)	-0.0228080(8)
	50	-0.01457976(5)	-0.0145752(6)
	70	-0.01074986(3)	-0.010749(2)
	90	-0.00853156(2)	-0.0085314(5)

Table V. Total energy per particle in Hartree for the polarized system of $N = 27$ particles. FN-DMC results are obtained using the method in Appendix D.